Self-Assembled Large-Area Annular Cavity Arrays with Tunable Cylindrical Surface Plasmons for Sensing

Haibin Ni, Ming Wang,* Tianyi Shen, and Jing Zhou

Jiangsu Key Laboratory on Optoelectronic Technology, School of Physical Science and Technology, Nanjing Normal University, Nanjing 210023, China

ABSTRACT Surface plasmons that propagate along cylindrical metal/dielectric interfaces in annular apertures in metal films, called cylindrical surface plasmons (CSPs), exhibit attractive optical characteristics. However, it is challenging to fabricate these nanocoaxial structures. Here, we demonstrate a practical low-cost route to manufacture highly ordered, large-area annular cavity arrays (ACAs) that can support CSPs with great tunability. By employing a sol−gel coassembly method, reactive ion etching and metal sputtering techniques, regular, highly ordered ACAs in square-centimeter-scale with a gap width tunable in the range of several to hundreds of nanometers have been produced with good reproducibility. Ag ACAs with a gap width of 12 nm and a gap height of 635 nm are demonstrated. By finite-difference time-domain simulation, we confirm that the pronounced dips in the reflectance spectra of ACAs are attributable to CSP resonances excited in the annular gaps. By adjusting etching time and Ag film thickness, the CSP dips can be tuned to sweep the entire optical range of 360 to 1800 nm without changing sphere size, which makes them a promising candidate for forming integrated plasmonic sensing arrays. The high tunability of the CSP resonant frequencies together with strong electric field enhancement in the cavities make the ACAs promising candidates for surface plasmon sensors and SERS substrates, as, for example, they have been used in liquid refractive index (RI) sensing, demonstrating a sensitivity of 1505 nm/RIU and a figure of merit of 9. One of the CSP dips of ACAs with a certain geometry size is angle- (0−70 degrees) and polarization-independent and can be used as a narrow-band absorber. Furthermore, the nano annular cavity arrays can be used to construct solar cells, nanolasers and nanoparticle plasmonic tweezers.

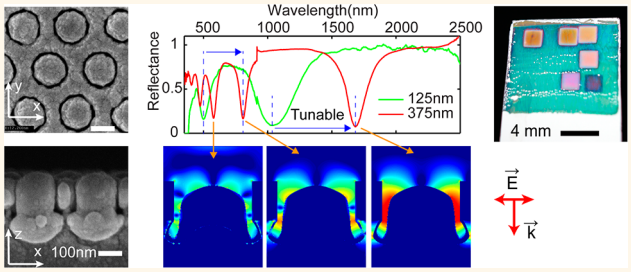

KEYWORDS: annular gap array · coaxial plasmonic structures · cylindrical surface plasmons · nanosphere lithography · self-assembly monolayer of nanospheres · SERS substrates · refractive index sensors

Confined to metal/dielectric interfaces, surface plasmons can afford strong electric field enhancement within the penetration depth of the evanescent wave, which is essential to increase most of light-matter interactions.[1−4] One significant and promising application of surface plasmons is used as chemical and biological sensors,[5−9] which has been intensively investigated in the past decades. According to propagating characters, surface plasmons are classed as two kinds: surface plasmon polaritons (SPPs) (or propagating surface plasmons) and localized surface plasmons (LSPs), which show distinct sensing performance. SPPs excited on continuous planar Au or Ag films can afford an extremely small detection limit exceeding 10^{-5} refractive-index units (RIU).[6] In contrast, LSPs formed in nanoarchitectures are less sensitive to refractive index changes with a sensitivity of about 1400 nm/RIU,[7] at least an order of magnitude lower than SPPs. However, LSPs can be directly excited in nanostructures, while SPPs usually need to be excited by other components with relatively large size. Thus, LSPs seem much more suitable for bulk sensitive applications. In addition, LSPs afford more tunability than SPPs,[10−13] which is desirable for some biosensing applications, such as surface enhanced Raman spectroscopy (SERS).[4] Nevertheless, higher tunability and sensitivity of LSPs based nanosensors are desired for many sensing applications.

In recent years, cylindrical surface plasmons (CSPs) excited in a nanoscale coaxial Au or Ag structure have attracted a wide research interest,[14−23] and these nanoscale plasmonic coaxial (NPC) structures capable

* Address correspondence to wangming@njnu.edu.cn.

Received for review December 1, 2014 and accepted February 1, 2015.

Published online February 01, 2015
10.1021/nn506834r

© 2015 American Chemical Society

of supporting CSPs have been applied to construct thresholdless nanolasers,[24] nanoparticle trapper,[25] color filter,[26] quarter-wave plates in visible range,[27] *etc.* A CSP can be directly excited as a guided mode in a NPC structure with modes far smaller than the CSP wavelength; moreover, the CSP wavelength can be continuously tuned by adjusting the geometry size of the coaxial structure, even increasing to infinitely large when the annular gap width decreases to infinitely small.[28−30] As a special case of SPPs, CSPs not only can be directly excited in NPC structures but also exhibit great tunability, which are two merits of a LSP. Hence, compared to previously reported LSP and SPP based sensors, NPC structures would show comprehensive performance as surface plasmon sensors. However, it is still hard now to produce NPC structures with narrow annular gaps though researchers are making efforts to overcome this challenge.[31,32] So far, the most widely adopted fabrication procedures to produce NPC structures all involves focused ion beam (FIB) or electron beam (EB) lithography method which is time-consuming and thus not suitable for mass manufacture.[33,34] In addition, the FIB/EB lithography method has a limitation of about 10 nm in the produced annular gap width for a thin metal film.[35] Creating a 10 nm-width gap in a thick metal film (more than 150 nm) is challenging for this method.

Without using FIB/EB lithography method, two kinds of coaxial structures fabricated by other methods have been reported. One is plasmonic core/shell nanorod arrays produced in an anodized aluminum oxide template by electrochemical grown method.[6,36−38] The fabrication method is simple and with good reproducibility, and an extremely small gap (<10 nm) between a rod and shell can be formed. However, the guided mode supported in this kind of array which shows an extremely high sensitivity of about 32 000 nm/RIU needs to be excited by a prism. Another kind is vertical oriented coaxial structure arrays fabricated by a series of complex procedures, including atom layer deposition (ALD) and nanosphere mechanical polishing monitored by a scanning electron microscope (SEM) that needs precision controlment.[39,40] Thus, this method is also not suitable for mass fabrication. Most importantly, no CSP related properties of the two kinds of coaxial structures have been reported. Therefore, to fabricate NPC structures that can support tunable CSPs, a low cost, reproducible method that is suitable for mass fabrication and capable of producing narrow gaps in thick films is highly desired. As a low-cost nanofabrication method, nanosphere lithography (NSL) method has been widely applied to produce a variety of two-dimensional periodic plasmonic structures with large tunability and good reproducibility recently.[11,41,42] Combined with the ALD method, even a 10 nm gap is realized by NSL method.[7] Thus, we focus on utilizing the NSL method to construct NPC structures for sensing.

In this work, we report a novel route for the high-throughput, reproducible fabrication of periodic arrays of annular cavities (ACAs) with controlled gap width, depth and gap radius by the NSL method. The fabrication mechanisms, parameters and their influence on geometry size of produced ACAs are discussed. Polystyrene (PS) spheres ranging from 250 to 690 nm in diameter have been demonstrated to fabricate high-quality, large-area ACAs with great geometry size tunability. Multiple surface plasmon resonances can be directly excited in the resultant ACAs by incident light. Using finite-difference time-domain (FDTD) simulation, we confirmed that the pronounced dips in the reflection spectra of ACAs are attributed to CSPs. Furthermore, an optimal range of fabrication parameters and influence of geometry size on CSP dips were investigated. Also angle- and polarization-dependent properties of CSP dips in ACAs with varied geometry size were measured. In the end, we investigated the sensing performance of ACAs as liquid refractive index (RI) sensors and as SERS substrates for adenine detection. An RI sensitivity of 1505 nm/RIU and a figure of merit (FOM) of 85 were obtained.

RESULTS AND DISCUSSION

Fabrication Mechanisms and Morphologies of Fabricated ACAs. To fabricate ACAs, we used the NSL method, which involves hexagonal packing of PS spheres with partially infiltrated silica gel, oxygen reactive ion etching (RIE) and silver (Ag) film deposition. As depicted schematically in Figure 1a, the fabrication process consists of three steps. PS spheres were self-assembled into a monolayer of hexagonal arranged arrays using the sol−gel coassembly method,[43] silica gel in solution was infiltrated in the interstitials of these spheres spontaneously, which resulted in PS sphere arrays partially embedded in silica gel, as shown in Figure 1a and Figure S1a,b (Supporting Information). This monolayer periodic PS sphere and silica gel composite film will be referred to as PSC film in the following text. The infiltrated silica gel plays a significant role in the formation of annular cavities in the followed fabrication process. Overall geometry sizes of the ACAs are characterized in 1b. SEM images of the fabricated ACAs are shown in Figure 1c−e,g,h, in which the cap-like Ag patches coated on partially etched PS spheres formed the inner edges of the gaps and their outer edges were defined by mesh-like Ag film on silica gel. The formed gap width can be as small as ∼12 nm (see Figure 1d,e), whereas the gap height is larger than 100 nm for D = 250 nm. Height of the fabricated annular gap can reach approximately 635 nm with an average gap width of ∼30 nm for D = 690 nm (see Figure 1g). Highly ordered ACAs with areas in square-centimeter range can be produced by this method (see Figure 1f,i). The geometry sizes and area of ACAs can be further improved by employing optimized fabrication

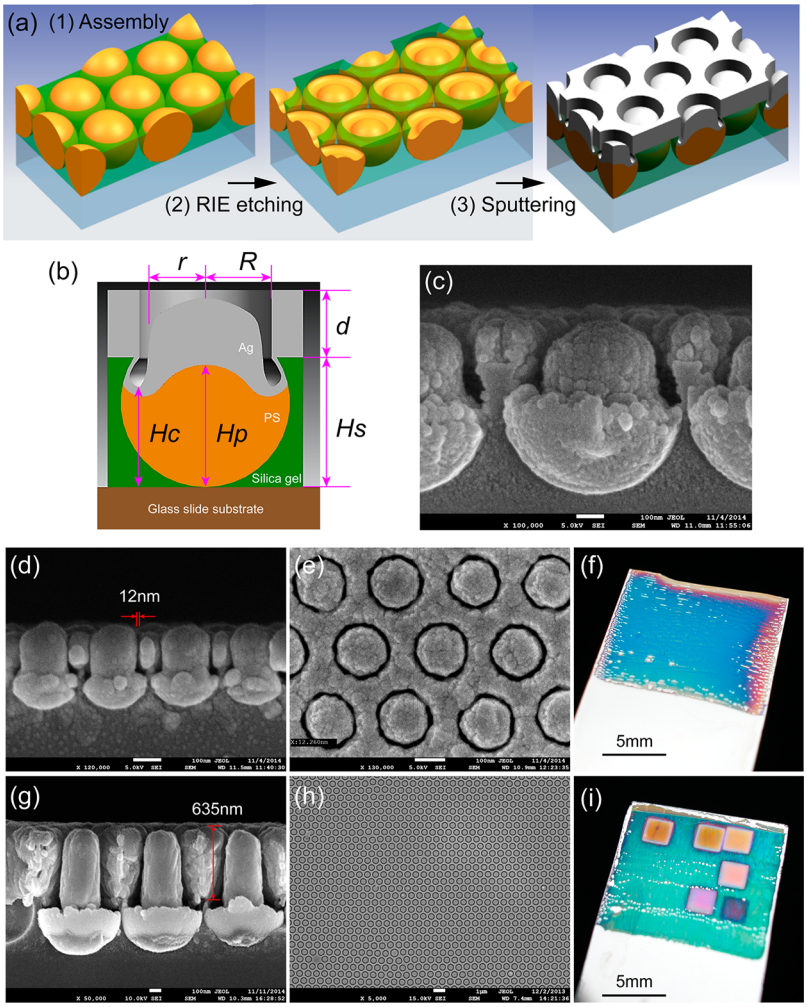

Figure 1. Annular cavity arrays (ACAs). (a) Schematic of the fabrication process for ACAs using a sol–gel nanosphere coassembly method together with RIE and metal sputtering techniques. Initially, a monolayer of a periodic PS sphere array partially immersed in a thin layer of silica gel (the thickness of the silica gel is less than the sphere diameter) was prepared on a glass slide using a sol–gel coassembly method; then, isotropic etching of the PS spheres was performed using O_2 RIE to form annular gaps between the residual PS particles and surrounding silica gel, making the gap width proportional to the etching time. A layer of Ag film was then sputtered on the top surface of the etched PSC film. (b) Model of vertical cross section of the fabricated ACAs characterized by a film thickness *d*, gap outer radii *R*, gap inner radii *r*, silica gel infiltration height *Hs*, etched PS height *Hp*, cavity depth *Hc* and sphere diameter *D* (equal to the lattice constant of the hexagonal array). SEM images of the vertical cross section of ACAs fabricated with (c) RIE etching time $t = 10$ min, $d = 150$ nm and $D = 690$ nm, (d) $t = 220$ s, $d = 100$ nm and $D = 250$ nm, and (g) $t = 15$ min, $d = 635$ nm and $D = 690$ nm; scale bar is 100 nm. (e) Top-view SEM image and (f) photograph of Ag ACAs shown in (d); scale bars are 100 nm and 5 mm. (h) Large-area highly ordered ACAs with $t = 15$ min, $d = 175$ nm and $D = 690$ nm; the scale bar is 100 nm. (i) Photograph of ACAs fabricated on a slide with $d = 200$ nm and $D = 690$ nm. Six 2 mm squares exhibit different colors in the film corresponding to ACAs with different etching times $t = 3, 6, 9, 12, 15$, and 18 min, *i.e.*, different gap widths ($R - r$). The blue areas in the PSC film are treated with the same fabrication process as the six squares except without any O_2 RIE etching treatment. The scale bar is 5 mm.

conditions. In addition, ACAs with varied gap widths can be integrated in a minor area, as demonstrated in Figure 1i, which was fabricated from the same PSC film with different etching time using a square etching mask but underwent the same metal sputtering progress, *i.e.*, has the same Ag film thickness.

Influence of Fabrication Parameters on Geometry Size. To produce a gap with a high depth-width ratio between the PS spheres and surrounding silica gel, etching parameters were selected to etch the PS spheres isotropically while keeping the silica gel unchanged. Upon the initiation of oxygen etching, an annular gap formed along the borderline between PS spheres and silica gel. As the etching time *t* increased, the gap broadened in width and deepened in depth while the shape of the top part of the residual PS particles was approximately semispherical, as shown in Figure 2a–c and Figure S1c–h. Morphologies of the ACAs with varied *t* and *d* were examined by SEM, as shown in Figure 2d–l. As *t* increases, *r* decreases and *R* remains constant. Both *R* and *r* as well as the gap width ($R - r$) decreased when increasing *d* for a wide range of *t*. The inner cap-like Ag patches are slightly higher in height than the outer net-like Ag film,

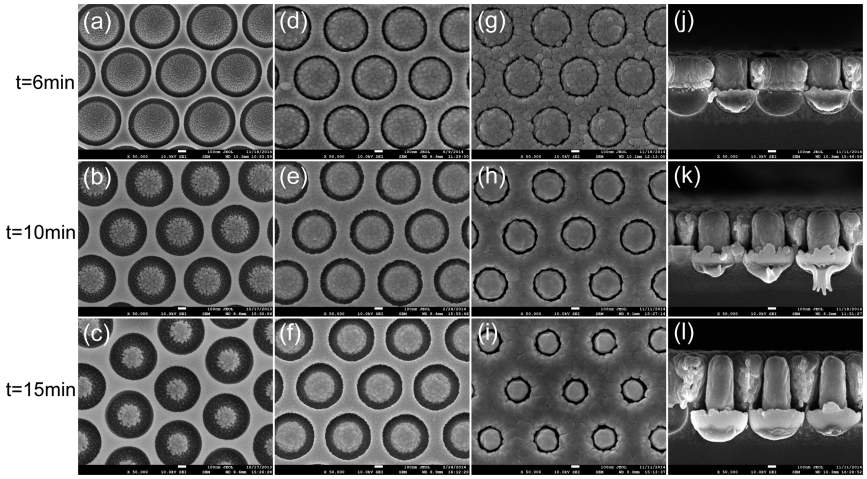

Figure 2. SEM images of the etched PSC film and ACAs with D = 690 nm. (a−c) Top view of the PSC film after oxygen RIE etching with t = 6, 10, and 15 min, respectively. (d−f) Top view of ACAs fabricated from the etched PSC film shown in (a−c) with d = 150 nm. (g−i) Top view of ACAs fabricated from the etched PSC film shown in (a−c) with increased d. (g) t = 6 min, d = 270 nm; (h) t = 10 min, d = 375 nm; and (i) t = 15 min, d = 635 nm. (j−l) SEM images show vertical cross section of the ACAs shown in (g−i), respectively. The scale bar is 100 nm in all SEM images.

with a height difference of ∼60 nm for t = 6 min, *i.e.*, $(Hp + d) - (Hs + d) \approx 60$ nm, whereas they are nearly the same height for t = 10 min and slightly lower for t = 15 min with ∼50 nm, *i.e.*, $(Hs + d) - (Hp + d) \approx 50$ nm. During the RIE etching process, Hc decreases by ∼16 nm per/min (see Figure S1c−e). In conclusion, R is dependent on d, Hs, and D, whereas r is mainly determined by t, d, Hs, and D. The gap width $(R - r)$ is determined by t, d, Hs and D. The height difference of the cap-like patches and net-like film are determined by t. Hc is dependent on t and, to a lesser extent, d.

To simplify discussion, infiltration degree of silica gel F, which determines the morphologies of PSC films and partially determines the resulted ACAs, defined as $F = Hs/D$, was held constant ($F \approx 0.768$) by using the same fabrication parameters to fabricate PSC films in this work. Thus, for a particular value of D, that is diameter of PS spheres, geometric features of the fabricated ACAs are only determined by fabrication parameters t and d, and they could be tuned precisely over a wide range.

Measured and FDTD Simulated Reflectance Spectra of ACAs. A typical measured reflectance spectrum of the ACAs (t = 10 min) at normal incidence is shown in Figure 3a. The noncontinuous point at λ = 915.6 nm is due to the combination of two spectra ranging from 350 to 1050 nm and 950 to 2500 nm, respectively. Three pronounced reflection dips located at wavelengths λ = 483, 664 nm (692 nm in simulation) and 1432 nm (1416 nm) are observed, which cannot be interpreted by the well-known surface plasmon theories, such as surface plasmon polariton Bloch wave (SPP-BW) or dipolar resonance of nanoparticles. To explore the nature of these dips, FDTD simulations were conducted using models with geometric size identical to those of the measured samples in experiments by commercial software (East FDTD, Dongjun technology, Shanghai, China).

Simulated reflectance spectrum also exhibits three dips, shown in Figure 3a, which is in good agreement with measured results. The slight discrepancy of the simulated dips at 692 and 1416 nm with measured ones is attributed to the minor geometric differences between the ideal simulation model and measured sample. Aside from three pronounced dips, there is another dip at λ = 592 nm in the simulation spectrum, which is attributed to Wood's anomaly (WA) as it is close to the theoretical value of (1, 0) WA at Ag/air interface given by $\lambda_{RA} = 2\pi(\varepsilon_{air})^{1/2}/G(1, 0) = 597.5$ nm ($G(1, 0)$ is the (1, 0) reciprocal vector of the hexagonal lattice). In addition, a shallow dip at 650 nm induced by the (1, 0) SPP-BW mode at Ag/air interface has been observed, which corresponds to the shallow dip at λ = 616 nm in the measured spectrum. Most of the measured reflectance spectra of ACAs exhibit a dip around λ = 620 nm regardless of etching time and Ag film thickness while the dip due to Wood's anomaly does not appear in the measured reflectance spectra.

In addition, reflectance spectra of ACAs at normal incidence with varied polarization directions are also simulated. Results indicate that polarization direction of normal incident light do not affect the reflectance spectra of ACAs, see Figure S2; that is, domain orientation of hexagonally arranged annular cavities do not affect the reflectance spectra.

Scalable Fabrication Parameters on PS Sphere Diameter. Reflectance spectra of ACAs fabricated from 250 nm-diameter PS spheres with t = 220 s and d = 100 nm (see Figure 1d−f) were also measured and simulated. As presented in Figure 3b, the first CSP dips are located at wavelengths of 600 and 800 nm when d is 50 and 100 nm, respectively. Because the fabrication parameters

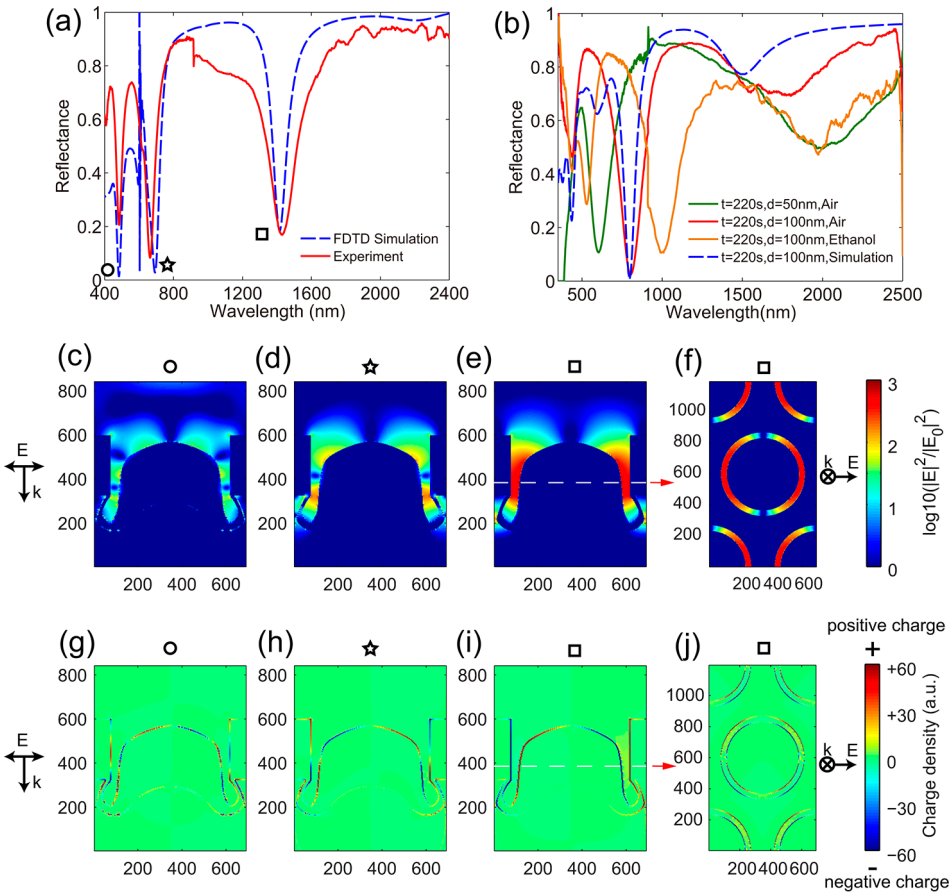

Figure 3. Measured and FDTD simulated optical properties of Ag ACAs. (a) Measured and simulated reflectance spectrum of ACAs with D = 690 nm (lattice constant of the hexagonal array), Hs = 530 nm, Hp = 500 nm, Hc = 400 nm, R = 270 nm, $r \approx$ 238 nm, d = 275 nm. (b) Measured reflectance spectra of ACAs fabricated from 250 nm-diameter PS spheres with d = 50 nm and d = 100 nm in air and in ethanol, and simulated reflectance spectrum of ACAs with d = 100 nm, t = 220 s and D = 250 nm. (c−e) Simulated electric field intensity enhancement factor distributions (normalized to electric field intensity of incident light) on a vertical cross section of the ACAs model used in (a) at λ = 483, 692 and 1416 nm, respectively, and (f) on a horizontal cross section of the ACAs model at λ = 1416 nm, H = 363 (corresponding to the longitudinal coordinates in (e)). (g−j) Charge density distributions calculated from the electric field distributions shown in (c−f). Unit of the axes in (c−j) is 1 nm.

of this ACA with D = 250 nm are proportional (250 nm/690 nm = 0.362) to that of ACAs with D = 690 nm (t = 10 min and d = 275 nm), we scale down the model used to simulate ACAs with D = 690 nm, t = 10 min and d = 275 nm to simulate the reflectance spectra of ACAs with D = 250 nm, t = 220 s, d = 100 nm. The simulated results correspond well with the measured results (see Figure 3b). Hence, the geometric size of ACAs could be approximately scaled down through decreasing D (with D in range of 250−690 nm) and using fabrication parameters proportional to D. In this work, to explore the characters of ACAs in optical (both the visual and NIR) domains, ACAs with D = 690 nm were mainly investigated. Thus, when not specifically indicated, D = 690 nm throughout this paper. Large-area SEM images of ACAs with D = 250 nm are shown in Figure S3.

FDTD Simulated Electric Field and Charge Density Distributions in ACAs. To reveal the origin of the three pronounced dips, an electric field distribution was simulated at each dip wavelength and is presented in Figure 3c−e in the form of the intensity enhancement factor, $\eta = \log_{10}(|E|^2/|E_0|^2)$, where $|E_0|^2$ is the incident wave intensity. A strong electric field enhancement (max $|E|^2/|E_0|^2$ = 1065, at λ = 1416 nm) was observed in the cavity gaps at each dip wavelength. In addition, the number of electric field enhancement nodes, *i.e.*, resonance nodes, along the cavity depth direction increased as the wavelengths of the dips decreased, similar to a Fabry−Perot interference that has formed in the depth direction of the cavity. To distinguish these dips, we named them the first, second and third dip according to the number of nodes along the cavity depth direction; for example, the dip at λ = 1416 nm with one node was named the first dip. However, two nodes may also occur along the gap depth direction when other types of surface plasmon resonances are excited, such as the excitation of dipolar resonance or SPP-BW in periodic metal/dielectric structures (see Figure S4d). To know whether these dips are related to SPP-BW, reflectance spectrum and electric field distribution of a single annular cavity at normal incidence is

simulated, as shown in Figure S5. Wavelengths of the reflectance dips and electric field distributions at these dips are the same as that of ACAs, only the first CSP dip shows a slight shift (~30 nm). Moreover, strong electric field enhancements still exist as evidenced by electric field distributions of ACAs at 30° incidence for both TE (s polarized wave) and TM (p polarized wave) polarization at wavelengths of the three pronounced dips (see Figure S6). Thus, the three dips are not induced by SPP-BW. In addition, cross-section charge density distributions at the three dips are calculated by solving divergence of the simulated electric field distributions shown in Figure 3c–f, see Figure 3g–j.

Physical Origin of the Pronounced Dips Presented in Reflectance Spectra. According to the above simulation results, the three surface plasmon resonances in the ACA are independent to periodicity and not dependent on incident angle at least in the range of 0–30°. In addition, considered the geometry size dependent, angle and polarization resolved optical reflectance spectra of ACAs which will be discussed below in detail, we confirm that the dips in reflectance spectrum of the ACA are attributed to CSP, and optical responses of ACAs are mainly dominated by CSPs. Furthermore, features of optical reflectance spectra, electric field and charge density distributions of ACAs with varied fabrication parameters (6 min $\leq t \leq$ 15 min) were compared with that of annular aperture arrays (AAAs), which capable of supporting CSPs and have been investigated intensively. As a result, all of them are quite similar (compare Figure 3, Figures S7 and S8 with Figure S4).

Optimal Range of Fabrication Parameters for ACAs to Support CSPs. Influence of the fabrication parameters (t, d) on the formation of CSP resonances was experimentally examined for the case of a PSC film with D = 690 nm, as shown in Figure 4a,b. Because gap width ($R - r$) decreases as d increases, the annular gap will close when d reaches a certain value which is small for short etching time. For an etching time t = 3 min, the first CSP dip disappeared when d reached ~175 nm (see Figure S9a,b), which resulted from the nearly closed annular gaps of the ACA. When t increased to 18 min, the formed annular cavities featured a large gap width and large height difference between both sides of the cavities because most part of PS spheres was etched, resulting in not strong CSPs and not good reflectance spectra (see Figure S9c,d and S10). Therefore, the optimal range of etching time is 6–15 min for the PSC films used here. With t in this range, there are several dips at ~610, 780, and 910 nm in the measured reflectance when d is 25 and 50 nm. The dips at ~610 and 910 nm correspond to the (1, 0) SPP-BW mode at the Ag/air interface and the (1, 0) SPP-BW mode at the Ag/silica interface, respectively, whereas the origin of the dip at ~780 nm is uncertain, and this dip did not shift as d increased. When t increased to 75 nm, the second CSP dip appeared at a wavelength of approximately 460 nm, whereas the first dip located at approximately 800 nm that is identifiable from other dips. Nevertheless, these CSP dips are shallow and broad due to the weak confinement of the gaps. Until d increased to 125 nm or larger, CSPs were effectively confined in the annular gaps, confirmed by the CSP dips that were steady in shape; furthermore, reflectance of the first CSP dip reached ~0.1 or less, depending on the particular geometry size. Thus, d = 125 nm was sufficient to form CSP dips with good performance for PSC with D = 690 nm and t in the range of 6–15 min. Proportionally, to effectively confine SPs in the gaps in PSC film with D = 250 nm, the required minimum d would be 45 nm, and it was confirmed by the measured reflectance spectrum of ACAs with d = 50 nm (see Figure 3b).

Dependence of Reflectance Spectra of ACAs on Geometry Size. Dependence of the CSP dips on geometric size of the ACAs in metal films with Drude-like dispersion has been investigated. Referring to size dependent laws of CSPs excited in AAAs, which are concluded in the literature,[28–30,44,45] we infer that the wavelengths of CSP dips of ACAs would be linearly dependent on the film thickness d and dependent on R and r. In particular, they would increase infinitely as $1/(R - r)^{1/2}$ when R and r approach each other. To verify these inferences, reflection spectra of ACAs with varied geometry size (d, r, and R) were simulated. The simulation results indicated that as Ag film thickness d increased, wavelengths of the CSP dips linearly increased (Figure 4c). With a decrease in the gap width ($R - r$), *i.e.*, R increases or r decreases, wavelengths of CSP dips increased in an approximately linear manner but tended to nonlinearity when ($R - r$) approached ~20 nm (Figure 4d and Figure S11). In addition, wavelengths of the CSP dips were also dependent on ($R + r$). CSP dips shifted to shorter wavelength as ($R + r$) decreased, which was confirmed by both simulation and experiments in cases where D decreased from 690 to 250 nm (see Figure 3a,b).

The experimentally measured reflectance spectra of ACAs with varied film thicknesses (d, r and R) are in coincidence with simulation results, which further confirms that the dips of ACAs are mainly ascribed to CSPs. As shown in Figure 4e and Figure S12, the measured CSP dips shifted to longer wavelength, and new dips continuously formed in the shorter wavelength as film sputtering time increased, *i.e.*, d increased, for t in the range of 6–15 min. Wavelengths of CSP dips are nearly linear in d when t = 10 min (for d in the range of 125–375 nm) and t = 15 min (for d in the range of 125–600 nm), whereas they were nonlinear for t = 6 min (for d in the range of 125–270 nm), as plotted in Figure 4f. The CSP dip could be tuned in a larger range with an increased film thickness. As noted previously, increase of d in a metal sputtering process

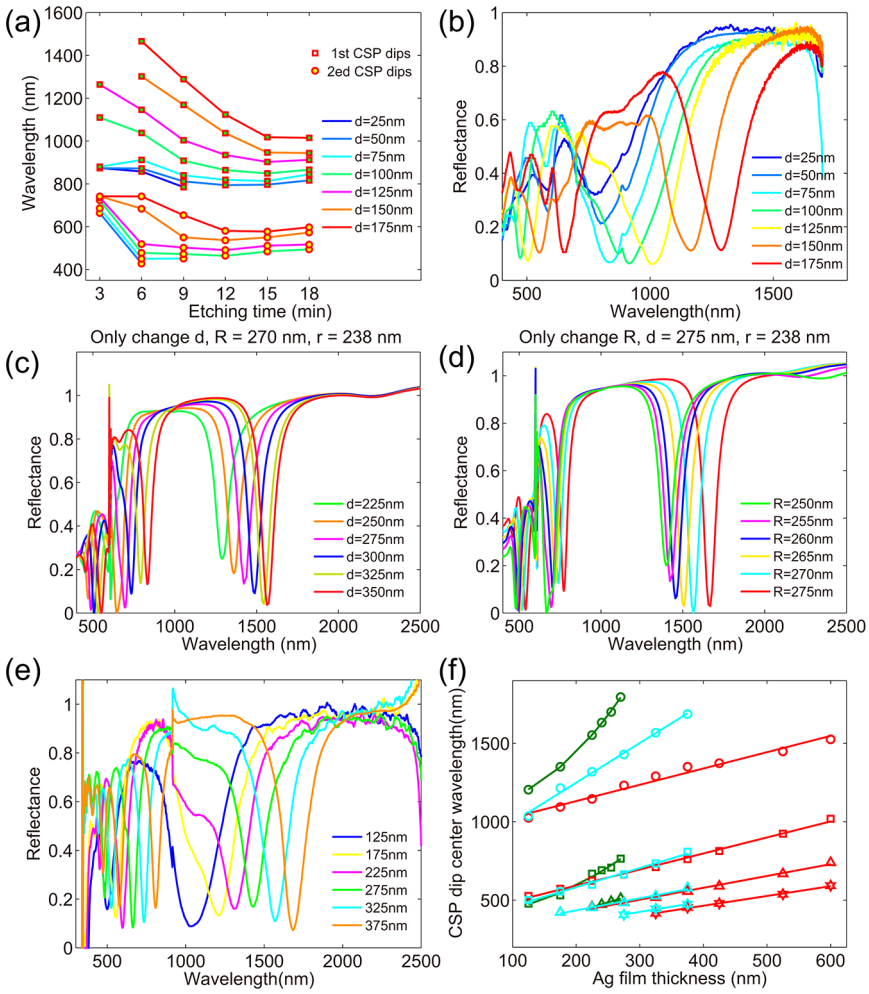

Figure 4. (a) Plot of the measured wavelengths of the first (squares) and second (circles) CSP dips of ACAs with various fabrication parameters, t = 3, 6, 9, 12, 15, and 18 min and d = 25, 50, 75, 100, 125, 150, and 175 nm. (b) Measured reflection spectra of ACAs (etching time t = 9 min) with the Ag film thickness varied in the range of 25−175 nm. FDTD simulated reflectance spectra of the model used in Figure 3a modified by (c) only adjusting the Ag film thickness d while keeping R and r constant and (d) only changing R while keeping the Ag film thickness d and r unchanged. (e) Measured reflection spectra of ACAs (etching time t = 10 min) with various Ag film thicknesses. The feature at a wavelength of 920 nm is caused by the combination of two spectra, which cover the short and long wavelength ranges, respectively. (f) Wavelengths of the CSP dips of ACAs with etching time t = 6 (green), 10 (cyan), and 15 min (red) and increased Ag film thickness. Circles, squares, triangles and hexagrams represent the first, second, third and fourth CSP dips in a measured reflectance spectrum, respectively.

would always accompanied by a decrease in the gap width ($R - r$), a major decrease in R and a minor decrease in r, as shown in Figure 2l at a cross section of t = 15 min. Thus, the shift of CSP dips in the experiments is attributed to the combined effect of changes in Ag film thickness d and gap width ($R - r$). However, as ($R - r$) cannot be quantitatively record conveniently in experiments, we used film thickness d here to represent the combined effect of both variations of d and ($R - r$) because the two variables are correlated in a degree. For the case of t = 10 min and t = 15 min, the gap width is sufficiently large (larger than ~25 nm) that the CSP dips on the inner and outer wall of cavities have less coherence for d in the measured range. For t = 6 min, the gap width is approximately 100 nm and ~20 nm (measured from SEM image) before and after sputtering a layer of 275 nm-thick Ag film, respectively, which resulted in a strong coherence between the CSPs on both cavity walls, *i.e.*, a small change in the gap width induced a large shift in the CSP dips. By ACAs, we first experimentally demonstrate the following: (i) multiple CSP resonances are excited in optical range, and (ii) a nonlinear dependency between the CSP resonant frequencies and gap width when the gap width is approaching 20 nm, which have been demonstrated by calculation and simulation in the previous reports.[28,30]

As shown in Figure 3b, the first CSP dip can also be tuned to the visible wavelength range by decreasing D, which makes ACAs more flexible to various applications because the first and second CSP dips exhibit different characteristics, such as near-field electric field distribution patterns, full width at half-maximum (fwhm) and angle-resolved properties, as discussed below.

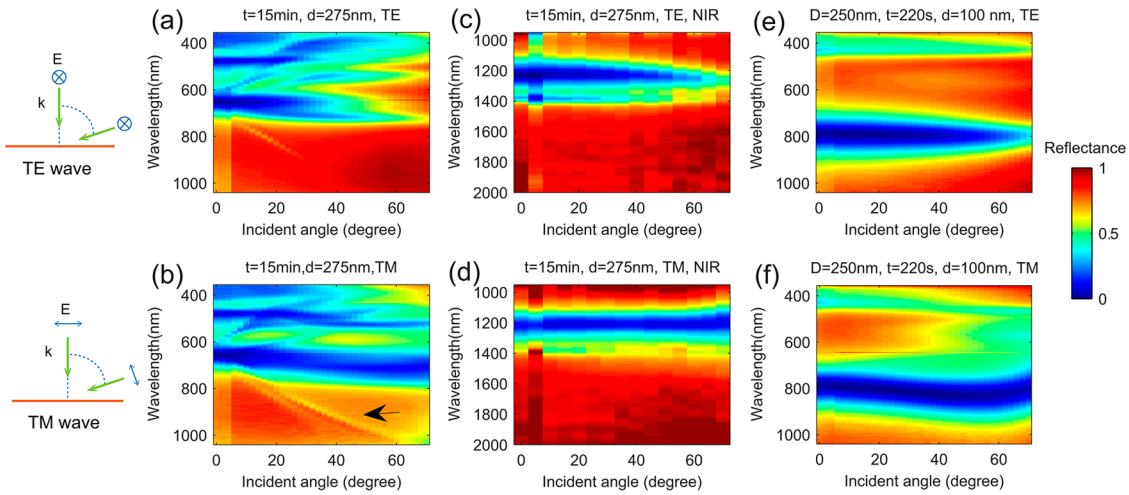

Figure 5. Measured angle- and polarization-resolved reflectance spectra map of ACAs with (a–d) t = 15 min, d = 275 nm, D = 690 nm and (e,f) t = 220 s, d = 100 nm, D = 250 nm. (a,c) TE polarization with angle resolutions of 2° and 5° for the short wavelength range (550–1050 nm) and long wavelength range (950–2000 nm), respectively. (b,d) TM polarization with angle resolutions of 2° and 5° for the short wavelength range (550–1050 nm) and long wavelength range (950–2000 nm), respectively. Black arrow drawn in (b) indicate the evolution of the dip attributed to the (1, 0) SPP-BW mode at the Ag/air interface with angle of TM polarized incident light. (e,f) TE and TM polarization with an angle resolutions of 2° in the wavelength range of 550–1050 nm, respectively.

Angle and Polarization Resolved Reflectance Spectra of ACAs with Varied Geometry Size. Evolution of reflectance spectra of ACAs with angle and polarization was experimentally investigated. As presented in Figure 5a–d, for ACAs with t = 15 min, d = 275 nm in the wavelength range of 550–2000 nm, the first CSP dip remains fairly constant as the angle of incident light varied from 0° to 70° for both TE and TM polarized light, whereas the second and third CSP dips are only retained in the range of 0° to ~30° for TE and TM polarized light. As the angle of incident light increased, new dips induced by the SPP-BW mode arose and appeared in the reflectance spectra maps (in the range of 400–1000 nm), as indicated by a black arrow in Figure 5b. The wavelengths of these dips are dependent on both the periodicity of the arrays, *i.e.*, D, (see Figure S13) and the angle of the incident light. Other dips around the second CSP dip arose in the spectra when the angle of incident light was larger than ~20°. These dips are attributed to the multipolar resonances of the cap-like Ag patches that were induced by the retardation effect.

As the thickness of Ag film increased, angle- and polarization-resolved reflectance properties with the same etching time did not change significantly, only the CSP dips were retained at a slightly larger angle range for both polarized incident lights (see Figure S13, t = 15 min, d = 525 nm). In contrast to the Ag film thickness, etching time show much more impact on those properties. For ACAs with t = 6 min and t = 10 min, the wavelengths of the first CSP dips shifted slightly as the angle of incident light varied in 0–70° for TM polarization while these dips were retained in a shorter angle range of 0–40° for TE polarization (see Figure S13). The reason for these differences might be ascribed to the height difference ($Hp - Hs \geq 0$ for t = 6 and 10 min, whereas $Hp - Hs < 0$ for t = 15 min) of the inner cap-like Ag patches and net-like Ag film (see Figure 2 j–l); this topic should be further investigated. The second and third CSP dips also disappear when the incident angle is larger than a particular degree ~20–30°, depending on the particular geometry size, for incident light of both TE and TM polarization. Compared to t = 10 min, dips that arise by Wood's anomaly and SPP-BW are more obvious for t = 6 min, which may be attributed to the more outstanding periodic features ($Hp - Hs > 0$). The angle- and polarization-resolved reflectance spectra of ACAs with D = 250 nm, t = 220 s, and d = 100 nm were also demonstrated with its first CSP dip located at λ = 800 nm (Figure 5e,f). The dip was slightly red-shifted as the incident angle increased for TM polarization because the inner patches were slightly higher than the outer net-like Ag film (see Figure 1d). To conclude, the geometry size of the ACAs impacts their angle- and polarization-dependent characters, and the angle-related performance of each CSP dip in a reflectance spectrum is different. The wide-angle (at least 0–70°) and polarization-independent properties of the first CSP dip located in the visual and NIR ranges can be obtained in ACAs with optimized geometric parameters.

Liquid Refractive Index Sensing. To explore the influence of the geometry size of ACAs on the liquid refractive index (RI) sensing performance, reflectance spectra of ACAs fabricated with etching time t = 6, 10, and 15 min together with different Ag film thicknesses in liquids of varied refractive indices were measured. The measured wavelengths of the first and second CSP dips were nearly linearly correlated with RI in the range of 1.3000–1.4725 for all of the samples with different t and d (see Figure 6a,b). The refractive index

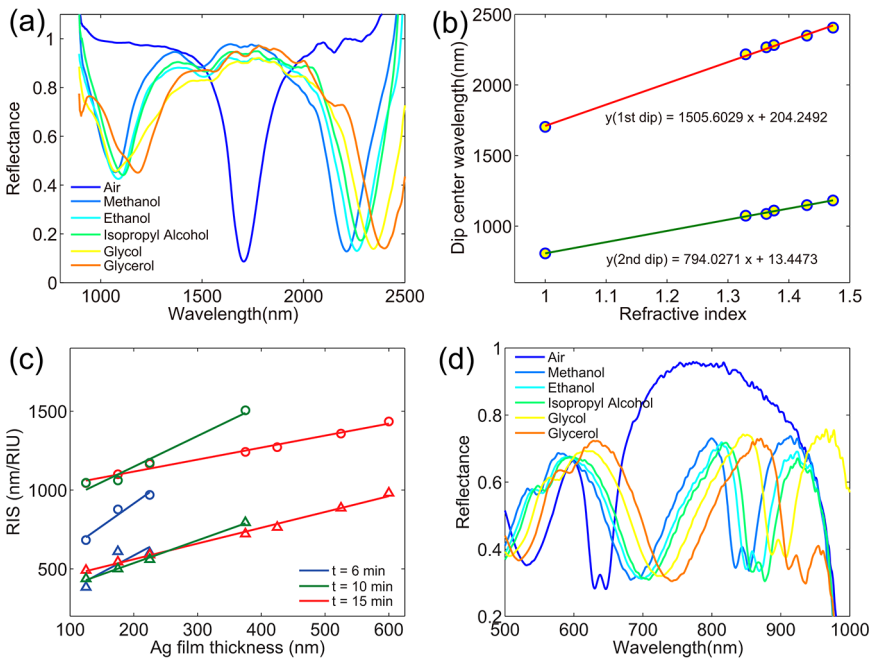

Figure 6. Measured refractive index sensing characters of ACAs. (a) Responses of the first CSP dip of ACAs (t = 10 min, d = 375 nm) immersed in liquids of different refractive indices. (b) Measured wavelengths of the first (red) and second (blue) CSP dips of ACAs (t = 10 min, d = 375 nm) *versus* refractive indices and their linear fit lines. (c) Measured refractive index sensitivity of ACAs with t = 6 (blue), 10 (cyan) and 15 min (red) as a function of film thickness d. Circles reresent the measured first CSP dips and triangles represent the measured second CSP dips. (d) Measured reflectance spectra of ACAs (t = 6 min, d = 175 nm) *versus* refractive indices. Partially overlap of the dip attributed to the (1, 0) SPP-BW mode at the Ag/air interface and one of the CSP dips at ~630 nm forms two dips with reduced fwhm and thus result in a high FOM.

sensitivity (RIS) also increased linearly with Ag film thickness for different t (6, 10, and 15 min), but the slopes of RIS to Ag film thickness decreased as t increased, as shown in Figure 6c. According to the electric field distribution of ACAs (Figure 3c), ACAs are mainly sensitive to liquids that are infiltrated in the annular gaps, and the locations in the gaps sensitive to liquid RI are different for different CSP dips. Characteristics that are commonly used to evaluate the performance of RI sensors are RIS, contrast ratio (CR, calculated as $(R_{max} - R_{min})/(R_{max} + R_{min})$), and FOM (calculated as RIS/fwhm). The highest RIS measured was 1505 nm/RIU with CR = 82% and FOM = 9 for ACAs with t = 10 min, d = 375 nm, and the RIS can further increase by increasing d. Ag film thickness was not further increased in experiments due to the detection limit of optical spectrum analyzer used.

Moreover, the FOM of ACAs can be easily tuned to 85, which is larger than the typically reported values of no more than 30.[8] Two ways are usually adopted to achieve high FOM: (i) decrease the fwhm of the dip or peak and (ii) increase the RIS. Due to the detection wavelength range of OSA, it is desirable to obtain high FOM with appropriate RIS for RI sensors, *i.e.*, minimize the fwhm. Fano resonance is an effective approach to decrease the fwhm of SP dips or peaks.[12,46−53] Recently, a SP-based RI sensor with an FOM as high as 105 through Fano resonance of the RA anomaly mode and F−P-like mode has been reported (with dip fwhm = 10 nm).[8] Similarly, we also find in reflectance spectra of ACAs that the dip induced by the (1, 0) SPP-BW mode at the Ag/air interface, and one of the CSP dips would overlap each other partially at a particular geometry size, which can decrease the fwhm of the involved CSP dip and the SPP-BW dip and thus dramatically increase the FOM. An ACA sample with an FOM value as high as 85 was demonstrated, with fabrication parameters of t = 6 min, d = 175 nm, D = 690 nm. As shown in Figure 6d, the fwhm of the SPP-BW-induced dip (dip wavelength = 620 nm) was decreased to 7 nm and the dip RIS = 597 nm/RIU. Compared to the complex measurement configuration in ref 8, which required polarized light with a tilted incident angle of 37.5° to achieve the high FOM, ACAs only need to measure the reflection spectrum at normal incidence with nonpolarized light. In addition, considering the angle-independent properties of the CSP dips, the RIS of liquids would also be independent of incident light. Nevertheless, the CR of this narrowed dip is reduced to only 7%, which may not adequate for some practical applications. A compromise between CR and FOM could be achieved by adjusting the coupling strength between the SPP-BW mode-induced dip and the CSP dip. A dip with CR = 45% and FOM = 30 (dip RIS is 609 nm/RIU) is demonstrated in Figure S14d, and the ACA sample structure parameters are t = 15 min, d = 600 nm, and D = 690 nm. Compared with other nanostructures with similar sensing principles,

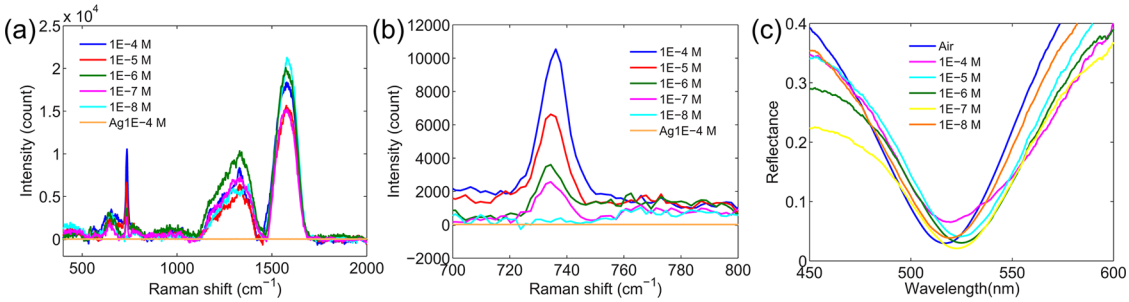

Figure 7. Performance of ACAs as SERS substrates. (a) Measured SERS signals from ACAs (t = 15 min, d = 125 nm), which were exposed to adenine-water solutions with different concentrations for 1 h. (b) Magnification of the spectra (a) at the 731 cm^{-1} shift. (c) Reflectance spectra of the ACAs before and after immersion in the adenine solution.

RI sensing characters of ACAs are quite competitive for their comprehensive performance of large RIS, FOM and CR, and most importantly, they all can be tuned in a wide range.

Used as SERS Substrates. ACAs as SERS substrates were also demonstrated. Adenine, a common biological molecule, was chosen to demonstrate the SERS enhancement ability of ACAs. Generally, an enhancement factor was used to evaluate the performance of SERS substrates; however, considering the surface area of ACAs and the per mm^2 number of molecules absorbed on the ACAs, it is difficult to estimate accurately. Thus, the limit of detection (LOD) of adenine was measured and compared with ref 7 to qualitatively demonstrate the SERS enhancement ability of ACAs. As wavelength of the exciting laser is 514.5 nm, one of the CSP dips was tuned to 514.5 nm by adjusting the film thickness in the fabrication process (see Figure S15). Figure 7a shows the measured SERS signals, and no SERS signals were detected from the ACAs immersed in solution with an adenine concentration of 1×10^{-8} M. Intensity of the purine stretch at 731 cm^{-1} shift was used to estimate the LOD (Figure 7b). Thus, LOD of the ACA sample for adenine is less than 1×10^{-7} M (100 nM), which is close to the value of 75 nM obtained in ref 7. This result can be attributed to the large mode volume with high electric field enhancement in the gaps. Ag film on slides with the same sputtering parameters immersed in 1×10^{-4} M were used as a comparison, but no SERS signals were detected from this film. After absorbing adenine molecules on the ACA surface, a maximum red shift of 7 nm of the CSP dip was observed for ACAs immersed in solution with a concentration of 1×10^{-4} M.

Compare with Other Methods and Structures. Compared to the FIB/EB method, the proposed NSL method is low-cost and high-productivity (producing large area samples) while it shows the same ability in fabricating annular gaps with gap width ranging from ~10 nm to several hundred nanometers as the FIB/EB method has. In addition, NSL method exhibits some advantages in producing narrow annular gaps in thick metal films. Compared to the Au nanorod array,[6,36] ACAs exhibit less sensitivity in biosensing but with significantly reduced size as CSPs can be directly excited by incident light in a wide incident angle in every single annular cavity, regardless of incident light polarization. Also CSPs in ACA can be tuned in a larger range than the tunable range of the guided surface plasmon in Au nanorods. In contrast to ACAs, vertically oriented coaxial tubes arrays,[39,40] fabricated by layer by layer film deposition and polishing method, can separate the coaxial tubes easily and make them in different materials with the cost of more complex fabrication procedures. Although they are major used as electrode-related applications now, vertically oriented coaxial tubes arrays might have potential to support CSPs, with optimal design, and may have similar performance as ACAs.

CONCLUSIONS

We have demonstrated a practical route to manufacturing ACAs with tunable reflection dips that originate from CSPs. By employing a NSL method with a sol−gel coassembly method and RIE and metal sputtering methods, highly ordered ACAs in a square-centimeter-scale with tunable gap width ranging from several to hundreds of nanometers have been produced with good reproducibility. The experimental ACAs possess several attractive properties: a strong electric field enhancement in the cavity gaps at CSP resonant wavelengths, great tunability of the multiple CSP resonant wavelengths that can sweep the entire visual and NIR wavelength range and angle- and polarization-independent properties of the first CSP dip at a particular geometry size. These properties make them applicable to multiple applications, such as surface plasmon sensors and SERS substrates, which we have demonstrated in this work and exhibit improved performance compared to that of previously reported nanostructures, and visual and NIR absorbers, solar cells, nanolasers, nanoparticle plasmonic tweezers, nanoreactive cavities and optical filters. In addition, because the tunability of ACAs can be achieved without changing the sphere size, *i.e.*, tuning the RIE etching time and sputtered Ag film thickness, ACAs with the same periodicity but different optical

properties (*i.e.*, different structure parameters, such as etching time, gap width and film thickness) can be manufactured on a minor chip using the integrated circuit (IC) fabrication process, which means that integrated plasmonic sensing chips based on ACAs can be produced conveniently in industry. Furthermore, ACAs might have the potential to be used as basic elements for integrated photonics chips, similar to transmitters for ICs. Improving the monolayer sphere arrangement technique and efficiency could further promote ACAs based devices adaptable to industry manufacture process for widespread use.

METHODS

Fabrication of Silver ACAs. Initially, a monolayer of hexagonally arranged composite PS sphere/silica gel arrays was formed by a sol−gel coassembly method previously reported by Hatton *et al.*,[43] but we adjusted the solution concentration to obtain a large-area monolayer of PSC. Standard glass slides were cleaned with a volume ratio of 3:7 solution of H_2O_2:H_2SO_4 for 1 h at 90 °C, followed by rinsing with DI water and drying with N_2 gas. The slides were treated with oxygen plasma under mild conditions (Harrick Plasma Cleaner, PDC-002, USA) for 10 min before use. Six milliliters of DI water was added to 20 μL of polystyrene microsphere suspension with a sphere diameter of 690 nm (10 wt %, Bangs Laboratories Incorporated, USA) and 20 μL of hydrolyzed tetraethyl orthosilicate (TEOS) solution (98%, Sigma-Aldrich), and the resulting solution was treated with sonication for 5 min at room temperature to form the mixed suspension for assembly. For the 250 nm PS sphere, the volume ratio for DI water, PS suspension and TEOS solution is 6 mL:10 μL:10 μL. The TEOS solution consisted of a 1:1:1.5 ratio by weight of TEOS (98% Aldrich), 0.1 M HCl, and ethanol (99.9%), respectively, and was stirred at room temperature for 1 h prior to use. A piece of cleaned slide was vertically immersed into the mixed suspension and fixed. Then, the suspension was placed in an oven for evaporation with the temperature set at 45 °C ± 1 °C. After the suspension was evaporated, a monolayer of PSC film was formed on the slide. Then, the slide with PSC film was treated with O_2 reactive ion etching (RIE) (150 W, 80 sccm) to partially remove the PS spheres. The residual PS morphology was dependent on the etching time *t*. For PS spheres in a 690 nm diameter, different *t* values were applied, such as 3, 6, 9, 10, 15, and 18 min. For samples made from PS spheres with a 250 nm diameter, *t* was 220 s. The RIE etched PSC film was sputtered with a layer of Ag film (0.025 Torr, Ar, 2.5 sccm), and the sputtered film thickness *d* was monitored by a quartz oscillator at an Ag deposition rate of ∼0.4 nm/s. A 300 μm-thick Al_2O_3 slice with a 2 mm × 2 mm square opening aperture was used as an RIE mask for selective etching of the PSC film. The morphology of the fabricated samples was characterized by scanning electron microscopy (JSM 7610F, JEOL, Japan). A thin layer of Pt film was sputtered on the samples to increase conductivity of the sample surface prior to SEM characterization.

Optical Characterization. Reflection spectra of ACAs covering the range of 360−2500 nm were measured by optical spectrum analyzers (OSAs) (Ocean optics, USB 2000, 360−1100 nm, NIRQUEST256, 950−2500 nm; and Yokogawa AQ6370, 600−1700 nm, Japan) and a 200-μm-core diameter reflectance probe (Ocean Optics). The data for the respective wavelength regions were combined to yield one reflectance spectrum covering 360−2500 nm. A white light source (Yokogawa AQ4305, 50 W, Japan) was coupled to six fibers in the reflectance probe and was normally projected to the surface of ACAs, with the reflected light collected by another fiber in the middle of the six fibers and sent to the OSA for recording. All spectra were normalized with respect to the spectrum measured from the Ag film, which was produced under the same sputtering conditions on a clean slide. A Yokogawa AQ6370 was used to measure the reflection power with high sensitivity. The angle-resolved reflection spectrum was measured using an angle-resolved measuring system (R1-A-UV, Fuxiang, China). The resolution of the angle in the measurement is 2° for the 400−1100 nm range and 5° for the 950−2500 nm range. Polarization controllers (550−1500 nm, 650−2000 nm) were introduced to control the polarization of the incident light. The transmission spectra of ACAs shown in Figure S16 were measured by a Cary 5000 (VARIAN, America) with a spot size of 1 mm in diameter.

FDTD Simulation. The simulation area consisted of one complete sphere and four quarters of spheres with periodic boundary conditions in the *y* and *z* directions in a plane parallel to the substrate, perfectly matched layer boundaries in the *x* direction perpendicular to the substrates, and a spatial grid of 3 nm in the *x*, *y* and *z* directions. A linearly polarized light pulse was impinged on the ACAs from the air side at normal incidence (along the *x* direction). In all simulations, the dielectric constants of the glass substrates, PS spheres, silica gel and air were set as 2.25, 2.434, 2.25 and 1, respectively, and the Drude−Lorentz model was used to fit the dielectric constant of Ag in the 300−2500 nm range. For a single annular cavity model, perfectly matched layer boundaries in the *x*, *y* and *z* direction were used.

Raman Spectroscopy. A newly fabricated ACA ($d \approx 125$ nm, $t = 15$ min) on a slide was cut into several pieces with width of 3 mm and immersed in adenine solutions with a concentrations of 1×10^{-8}, 1×10^{-7}, 1×10^{-6}, 1×10^{-5}, and 1×10^{-4} M for 1 h prior to SERS measurements. The samples were rinsed with DI water for 5 min and N_2-dried. A Labram HR800 measuring system equipped with a 514.5 nm argon-ion laser as an excitation light source was used to conduct the SERS measurement. A 20× objective lens was used to focus light on the sample with an incident light power of approximately 2 mW. The spot size is tens of micrometers. The accumulation time for the SERS signal is 45 s for all measurements.

Refractive Index Sensing. On the basis of the reflectance spectra measuring system, liquids were dripped on the ACA samples and then covered with a coverslip. After each measurement, the sample was rinsed with ethanol and air-dried. The reflection spectra were also normalized with respect to a measurement of bare Ag film on clean slides with the same deposition parameters.

Conflict of Interest: The authors declare no competing financial interest.

Acknowledgment. We would like to thank Li Long for the technique support in the sample preparation and associate professor Si Lin for the sample characterization by SEM. Also we would like to thank Yao Jie for helpful discussion. This work is supported by the National Natural Science Foundation of China (Grant Nos. 61178044 and 91123015), the Specialized Research Fund for the Doctoral Program of Higher Education (20113207110004), the Jiangsu Province Prospective Joint Research Project (BY2012005) and a project funded by the Priority Academic Program Development of Jiangsu Higher Education Institutions (PAPD).

Supporting Information Available: SEM images of the cross section/top view of PSC film and ACAs, simulated reflectance spectra of ACAs at normal incidence with different polarization directions, simulated results of AAA, simulated results of a single annular cavity, simulated electric field intensity distributions of ACAs at 30° tilted incident light, simulated results of ACAs with varied *t* and *d*, measured reflectance spectra of ACAs with varied *t* and *d*, measured angle- and polarization-dependent reflectance spectra of ACAs with varied *t* and *d*, transmission spectra of a ACA. This material is available free of charge *via* the Internet at http://pubs.acs.org.

REFERENCES AND NOTES

1. Meinzer, N.; Barnes, W. L.; Hooper, I. R. Plasmonic Meta-Atoms and Metasurfaces. *Nat. Photonics* **2014**, *8*, 889–898.
2. Zhou, W.; Dridi, M.; Suh, J. Y.; Kim, C. H.; Co, D. T.; Wasielewski, M. R.; Schatz, G. C.; Odom, T. W. Lasing Action in Strongly Coupled Plasmonic Nanocavity Arrays. *Nat. Nanotechnol.* **2013**, *8*, 506–511.
3. Kauranen, M.; Zayats, A. V. Nonlinear Plasmonics. *Nat. Photonics* **2012**, *6*, 737–748.
4. Lim, D.-K.; Jeon, K.-S.; Hwang, J.-H.; Kim, H.; Kwon, S.; Suh, Y. D.; Nam, J.-M. Highly Uniform and Reproducible Surface-Enhanced Raman Scattering from DNA-Tailorable Nanoparticles with 1-nm Interior Gap. *Nat. Nanotechnol.* **2011**, *6*, 452–460.
5. Chung, T.; Lee, S.-Y.; Song, E. Y.; Chun, H.; Lee, B. Plasmonic Nanostructures for Nano-Scale Bio-Sensing. *Sensors* **2011**, *11*, 10907–10929.
6. Kabashin, A. V.; Evans, P.; Pastkovsky, S.; Hendren, W.; Wurtz, G. A.; Atkinson, R.; Pollard, R.; Podolskiy, V. A.; Zayats, A. V. Plasmonic Nanorod Metamaterials for Biosensing. *Nat. Mater.* **2009**, *8*, 867–871.
7. Im, H.; Bantz, K. C.; Lee, S. H.; Johnson, T. W.; Haynes, C. L.; Oh, S.-H. Self-Assembled Plasmonic Nanoring Cavity Arrays for SERS and LSPR Biosensing. *Adv. Mater.* **2013**, *25*, 2678–2685.
8. Shen, Y.; Zhou, J.; Liu, T.; Tao, Y.; Jiang, R.; Liu, M.; Xiao, G.; Zhu, J.; Zhou, Z.-K.; Wang, X.; Jin, C.; Wang, J. Plasmonic Gold Mushroom Arrays with Refractive Index Sensing Figures of Merit Approaching the Theoretical Limit. *Nat. Commun.* **2013**, *4*, 2381.
9. Schmidt, M. A.; Lei, D. Y.; Wondraczek, L.; Nazabal, V.; Maier, S. A. Hybrid Nanoparticle−Microcavity-Based Plasmonic Nanosensors with Improved Detection Resolution and Extended Remote-Sensing Ability. *Nat. Commun.* **2012**, *3*, 1108.
10. Luk'yanchuk, B.; Zheludev, N. I.; Maier, S. A.; Halas, N. J.; Nordlander, P.; Giessen, H.; Chong, C. T. The Fano Resonance in Plasmonic Nanostructures and Metamaterials. *Nat. Mater.* **2010**, *9*, 707–715.
11. Heo, C.-J.; Kim, S.-H.; Jang, S. G.; Lee, S. Y.; Yang, S.-M. Gold "Nanograils" with Tunable Dipolar Multiple Plasmon Resonances. *Adv. Mater.* **2009**, *21*, 1726–1731.
12. Fan, J. A.; Bao, K.; Wu, C.; Bao, J.; Bardhan, R.; Halas, N. J.; Manoharan, V. N.; Shvets, G.; Nordlander, P.; Capasso, F. Fano-Like Interference in Self-Assembled Plasmonic Quadrumer Clusters. *Nano Lett.* **2010**, *10*, 4680–4685.
13. Sonnefraud, Y.; Verellen, N.; Sobhani, H.; Vandenbosch, G. A. E.; Moshchalkov, V. V.; Van Dorpe, P.; Nordlander, P.; Maier, S. A. Experimental Realization of Subradiant, Superradiant, and Fano Resonances in Ring/Disk Plasmonic Nanocavities. *ACS Nano* **2010**, *4*, 1664–1670.
14. Iwanaga, M.; Ikeda, N.; Sugimoto, Y. Enhancement of Local Electromagnetic Fields in Plasmonic Crystals of Coaxial Metallic Nanostructures. *Phys. Rev. B: Condens. Matter Mater. Phys.* **2012**, *85*, 045427.
15. Li, D.; Gordon, R. Electromagnetic Transmission Resonances for a Single Annular Aperture in a Metal Plate. *Phys. Rev. A: At., Mol., Opt. Phys.* **2010**, *82*, 041801.
16. Poujet, Y.; Salvi, J.; Baida, F. I. 9% Extraordinary Optical Transmission in the Visible Range through Annular Aperture Metallic Arrays. *Opt. Lett.* **2007**, *32*, 2942–2944.
17. Wang, X. K.; Xiong, W.; Sun, W. F.; Zhang, Y. Coaxial Waveguide Mode Reconstruction and Analysis with Thz Digital Holography. *Opt. Express* **2012**, *20*, 7706–7715.
18. Heshmat, B.; Li, D.; Darcie, T. E.; Gordon, R. Tuning Plasmonic Resonances of an Annular Aperture in Metal Plate. *Opt. Express* **2011**, *19*, 5912–5923.
19. de Waele, R.; Burgos, S. P.; Atwater, H. A.; Polman, A. Negative Refractive Index in Coaxial Plasmon Waveguides. *Opt. Express* **2010**, *18*, 12770–12778.
20. Baida, F. I.; Van Labeke, D. Light Transmission by Subwavelength Annular Aperture Arrays in Metallic Films. *Opt. Commun.* **2002**, *209*, 17–22.
21. Baida, F. I.; Poujet, Y.; Salvi, J.; Van Labeke, D.; Guizal, B. Extraordinary Transmission Beyond the Cut-Off through Sub-Lambda Annular Aperture Arrays. *Opt. Commun.* **2009**, *282*, 1463–1466.
22. de Waele, R.; Burgos, S. P.; Polman, A.; Atwater, H. A. Plasmon Dispersion in Coaxial Waveguides from Single-Cavity Optical Transmission Measurements. *Nano Lett.* **2009**, *9*, 2832–2837.
23. Wang, C. N.; Bai, M.; Jin, M. Enhanced Optical Transmission through Double-Overlapped Annular Aperture Array. *J. Mod. Opt.* **2012**, *59*, 1100–1105.
24. Khajavikhan, M.; Simic, A.; Katz, M.; Lee, J. H.; Slutsky, B.; Mizrahi, A.; Lomakin, V.; Fainman, Y. Thresholdless Nanoscale Coaxial Lasers. *Nature* **2012**, *482*, 204–207.
25. Saleh, A. A. E.; Dionne, J. A. Toward Efficient Optical Trapping of Sub-10-nm Particles with Coaxial Plasmonic Apertures. *Nano Lett.* **2012**, *12*, 5581–5586.
26. Liu, Y. J.; Si, G. Y.; Leong, E. S. P.; Xiang, N.; Danner, A. J.; Teng, J. H. Light-Driven Plasmonic Color Filters by Overlaying Photoresponsive Liquid Crystals on Gold Annular Aperture Arrays. *Adv. Mater.* **2012**, *24*, OP131–OP135.
27. Dahdah, J.; Hoblos, J.; Baida, F. I. Nanocoaxial Waveguide Grating as Quarter-Wave Plates in the Visible Range. *IEEE Photonics J.* **2012**, *4*, 87–94.
28. Fan, W.; Zhang, S.; Minhas, B.; Malloy, K. J.; Brueck, S. R. J. Enhanced Infrared Transmission through Subwavelength Coaxial Metallic Arrays. *Phys. Rev. Lett.* **2005**, *94*, 033902.
29. Baida, F. I.; Belkhir, A.; Van Labeke, D.; Lamrous, O. Subwavelength Metallic Coaxial Waveguides in the Optical Range: Role of the Plasmonic Modes. *Phys. Rev. B: Condens. Matter Mater. Phys.* **2006**, *74*, 205419.
30. Haftel, M. I.; Schlockermann, C.; Blumberg, G. Enhanced Transmission with Coaxial Nanoapertures: Role of Cylindrical Surface Plasmons. *Phys. Rev. B: Condens. Matter Mater. Phys.* **2006**, *74*, 235405.
31. Melli, M.; Polyakov, A.; Gargas, D.; Huynh, C.; Scipioni, L.; Bao, W.; Ogletree, D. F.; Schuck, P. J.; Cabrini, S.; Weber-Bargioni, A. Reaching the Theoretical Resonance Quality Factor Limit in Coaxial Plasmonic Nanoresonators Fabricated by Helium Ion Lithography. *Nano Lett.* **2013**, *13*, 2687–2691.
32. Jiang, X. X.; Gu, Q. C.; Wang, F. W.; Lv, J. T.; Ma, Z. H.; Si, G. Y. Fabrication of Coaxial Plasmonic Crystals by Focused Ion Beam Milling and Electron-Beam Lithography. *Mater. Lett.* **2013**, *100*, 192–194.
33. Si, G.; Zhao, Y.; Liu, H.; Teo, S.; Zhang, M.; Jun Huang, T.; Danner, A. J.; Teng, J. Annular Aperture Array Based Color Filter. *Appl. Phys. Lett.* **2011**, *99*, 033105.
34. Kofke, M. J.; Waldeck, D. H.; Fakhraai, Z.; Ip, S.; Walker, G. C. The Effect of Periodicity on the Extraordinary Optical Transmission of Annular Aperture Arrays. *Appl. Phys. Lett.* **2009**, *94*, 023104.
35. Si, G.; Zhao, Y.; Lv, J.; Wang, F.; Liu, H.; Teng, J.; Liu, Y. J. Direct and Accurate Patterning of Plasmonic Nanostructures with Ultrasmall Gaps. *Nanoscale* **2013**, *5*, 4309–4313.
36. Evans, P. R.; Wurtz, G. A.; Atkinson, R.; Hendren, W.; O'Connor, D.; Dickson, W.; Pollard, R. J.; Zayats, A. V. Plasmonic Core/Shell Nanorod Arrays: Subattoliter Controlled Geometry and Tunable Optical Properties. *J. Phys. Chem. C* **2007**, *111*, 12522–12527.
37. Atkinson, R.; Hendren, W.; Wurtz, G.; Dickson, W.; Zayats, A.; Evans, P.; Pollard, R. Anisotropic Optical Properties of Arrays of Gold Nanorods Embedded in Alumina. *Phys. Rev. B: Condens. Matter Mater. Phys.* **2006**, *73*, 235402.
38. Dickson, W.; Wurtz, G.; Evans, P.; O'Connor, D.; Atkinson, R.; Pollard, R.; Zayats, A. Dielectric-Loaded Plasmonic Nanoantenna Arrays: A Metamaterial with Tuneable Optical Properties. *Phys. Rev. B: Condens. Matter Mater. Phys.* **2007**, *76*, 115411.
39. Zhao, H.; Rizal, B.; McMahon, G.; Wang, H.; Dhakal, P.; Kirkpatrick, T.; Ren, Z.; Chiles, T. C.; Naughton, M. J.; Cai, D. Ultrasensitive Chemical Detection Using a Nanocoax Sensor. *ACS Nano* **2012**, *6*, 3171–3178.
40. Rizal, B.; Archibald, M. M.; Connolly, T.; Shepard, S.; Burns, M. J.; Chiles, T. C.; Naughton, M. J. Nanocoax-Based Electrochemical Sensor. *Anal. Chem.* **2013**, *85*, 10040–10044.

41. Bukasov, R.; Shumaker-Parry, J. S. Highly Tunable Infrared Extinction Properties of Gold Nanocrescents. *Nano Lett.* **2007**, *7*, 1113–1118.
42. Zhang, J.; Li, Y.; Zhang, X.; Yang, B. Colloidal Self-Assembly Meets Nanofabrication: From Two-Dimensional Colloidal Crystals to Nanostructure Arrays. *Adv. Mater.* **2010**, *22*, 4249–4269.
43. Hatton, B.; Mishchenko, L.; Davis, S.; Sandhage, K. H.; Aizenberg, J. Assembly of Large-Area, Highly Ordered, Crack-Free Inverse Opal Films. *Proc. Natl. Acad. Sci. U. S. A.* **2010**, *107*, 10354–10359.
44. Haftel, M. I.; Schlockermann, C.; Blumberg, G. Role of Cylindrical Surface Plasmons in Enhanced Transmission. *Appl. Phys. Lett.* **2006**, *88*, 193104.
45. Baida, F. I.; Van Labeke, D.; Granet, G.; Moreau, A.; Belkhir, A. Origin of the Super-Enhanced Light Transmission through a 2-D Metallic Annular Aperture Array: A Study of Photonic Bands. *Appl. Phys. B: Lasers Opt.* **2004**, *79*, 1–8.
46. Verellen, N.; López-Tejeira, F.; Paniagua-Domínguez, R.; Vercruysse, D.; Denkova, D.; Lagae, L.; Van Dorpe, P.; Moshchalkov, V. V.; Sánchez-Gil, J. A. Mode Parity-Controlled Fano- and Lorentz-Like Line Shapes Arising in Plasmonic Nanorods. *Nano Lett.* **2014**, *14*, 2322–2329.
47. Zhang, Y.; Jia, T. Q.; Zhang, H. M.; Xu, Z. Z. Fano Resonances in Disk-Ring Plasmonic Nanostructure: Strong Interaction between Bright Dipolar and Dark Multipolar Mode. *Opt. Lett.* **2012**, *37*, 4919–4921.
48. Fu, Y. H.; Zhang, J. B.; Yu, Y. F.; Luk'yanchuk, B. Generating and Manipulating Higher Order Fano Resonances in Dual-Disk Ring Plasmonic Nanostructures. *ACS Nano* **2012**, *6*, 5130–5137.
49. Cetin, A. E.; Altug, H. Fano Resonant Ring/Disk Plasmonic Nanocavities on Conducting Substrates for Advanced Biosensing. *ACS Nano* **2012**, *6*, 9989–9995.
50. Niu, L.; Zhang, J. B.; Fu, Y. H.; Kulkarni, S.; Lukyànchuk, B. Fano Resonance in Dual-Disk Ring Plasmonic Nanostructures. *Opt. Express* **2011**, *19*, 22974–22981.
51. Miroshnichenko, A. E.; Flach, S.; Kivshar, Y. S. Fano Resonances in Nanoscale Structures. *Rev. Mod. Phys.* **2010**, *82*, 2257–2298.
52. Lassiter, J. B.; Sobhani, H.; Fan, J. A.; Kundu, J.; Capasso, F.; Nordlander, P.; Halas, N. J. Fano Resonances in Plasmonic Nanoclusters: Geometrical and Chemical Tunability. *Nano Lett.* **2010**, *10*, 3184–3189.
53. Hao, F.; Nordlander, P.; Sonnefraud, Y.; Dorpe, P. V.; Maier, S. A. Tunability of Subradiant Dipolar and Fano-Type Plasmon Resonances in Metallic Ring/Disk Cavities: Implications for Nanoscale Optical Sensing. *ACS Nano* **2009**, *3*, 643–652.